Chemical Engineering & Processing: Process Intensification 124 (2018) 137–146

Contents lists available at ScienceDirect

Chemical Engineering & Processing: Process Intensification

journal homepage: www.elsevier.com/locate/cep

Kinetics model for the reduction of Fe_2O_3/Al_2O_3 by CO in Chemical Looping Combustion

Daofeng Mei[a,b,c], Haibo Zhao[a,*], Shuiping Yan[b,c]

[a] State Key Laboratory of Coal Combustion, Huazhong University of Science and Technology, Wuhan 430074, People's Republic of China
[b] Key Laboratory of Agricultural Equipment in Mid-lower Yangtze River, Ministry of Agriculture, Wuhan 430070, People's Republic of China
[c] College of Engineering, Huazhong Agricultural University, Wuhan 430070, People's Republic of China

ARTICLE INFO

Keywords:
Chemical looping combustion
Fe-based oxygen carrier
Nucleation and nuclei growth kinetics model
Diffusion model
Thermodynamics

ABSTRACT

Kinetics model which describes intrinsic characteristics of reactions involved in Chemical Looping Combustion (CLC) can be used as a basic tool for reactor design and reactor modeling. To further develop previously studied sol-gel Fe_2O_3/Al_2O_3 oxygen carrier, this work performed a detailed kinetics investigation for the reduction from Fe_2O_3/Al_2O_3 to Fe_3O_4/Al_2O_3 by CO. In order to derive a reliable kinetics model, thermodynamics calculations were first performed to identify the reaction pathways with full CO_2 capture and no carbon deposition, excluding their influence. Experimental data at 673–773 K during thermogravimetric analyzer (TGA) tests was considered for kinetics analysis to attain good CLC performance. Finally, a widely used model-free method was employed to develop the kinetics model. Accordingly, a 3D nucleation and nuclei growth model with the model function $g(X) = [-\ln(1-X)]^{1/3}$, activation energy 270 kJ/mol and pre-exponential factor $1.6{\cdot}10^{12}s^{-1}$ was developed to describe the first half reduction from Fe_2O_3/Al_2O_3 to Fe_3O_4/Al_2O_3 by CO ($0 < X \leq 0.5$). Following this, the diffusion effects dominated the reduction process ($0.5 < X \leq 1$), which can be described by a 2D diffusion model function $g(X) = (1-X)\cdot\ln(1-X) + X$ with the activation energy and pre-exponential factor as 131 kJ/mol and $3.1{\cdot}10^3\ s^{-1}$, respectively. The whole kinetics model can be considered for the future application.

1. Introduction

The global energy requirement still depends highly on the transformation of fossil fuels, which results in the continuing increase of CO_2 emissions [1]. The impact of CO_2 level on the average temperature of Earth is crucial, since it is considered as the largest contributor to the greenhouse effect [2,3]. In order to mitigate CO_2 emission, clean combustion technologies for fossil fuels were developed in the past decades. Among them, Chemical Looping Combustion (CLC) has emerged as a most competitive technology due to its low cost for CO_2 capture [4]. The CLC concept based on the ideas of producing pure CO_2 [5] and improving thermal efficiency via intermediate reactions [6] was first introduced by Ishida et al. [7] to reduce exergy loss. Different to conventional combustion, CLC avoids the direct contact between combustion air and fuel (C_nH_{2m}) through the transportation of oxygen carrier (MeO_x), usually metal oxides, between air reactor (AR) and fuel reactor (FR). The oxygen carrier provides lattice oxygen for the combustion of fuel via reaction R1 in FR, where the oxygen carrier is converted to a reduced state (MeO_{x-1}). Then, MeO_{x-1} is circulated to the AR to regenerate via reaction R2, ready for new cycles. Theoretically, the gas stream at the outlet of FR contains only CO_2 and H_2O, where the separation of H_2O from CO_2 can be easily accomplished through a simple condensation process. In this way, high-energy penalty is prevented for the CO_2 separation in CLC with respect to the other CO_2 capture technologies.

$$C_nH_{2m} + (2n + m)MeO_x \rightarrow (2n + m)MeO_{x-1} + nCO_2(g) + mH_2O(g) \quad (R1)$$

$$MeO_{x-1} + 1/2O_2(g) \rightarrow MeO_x \quad (R2)$$

Oxygen carrier is a cornerstone for the CLC process, which has to efficiently accomplish the task of oxygen transference between AR and FR. Among the more than 700 oxygen carriers developed to date [8], Fe-based oxygen carriers have high potentials due to the characteristics of low cost, environmental friendliness, low agglomeration tendency and low attrition rate. In the published works, Fe-based oxygen carriers mainly include synthetic materials, minerals and industrial wastes. Regarding the latter two cases, extensive investigations were carried out [9–16], especially for ilmenite minerals which were recently considered for the scale-up to 50kW–1 MW pilot plants for CLC [12,13]. In comparison to the synthetic oxygen carriers, minerals and industrial

* Corresponding author.
E-mail addresses: hzhao@mail.hust.edu.cn, klinsmannzhb@163.com (H. Zhao).

https://doi.org/10.1016/j.cep.2017.12.013
Received 10 March 2017; Received in revised form 19 December 2017; Accepted 20 December 2017
Available online 23 December 2017

Nomenclature

A	Pre-exponential factor, s^{-1}
C_nH_{2m}	Fuel
E	Activation energy, kJ/mol
$f(X)$	Differential form of reaction mechanism function
$g(X)$	Integral form of reaction mechanism function
m	Instantaneous mass of oxygen carrier, kg
MeO_x	Fully oxidized oxygen carrier
MeO_{x-1}	Fully reduced oxygen carrier
m_{ox}	Weight of completely oxidized oxygen carrier particles, kg
m_{red}	Weight of completely reduced oxygen carrier particles, kg
R	Universal gas constant, J/(mol K)
r^2	Linear coefficient
R_{OC}	Oxygen transport capacity
t	Reaction time, s
T	Temperature, K
X	Oxygen carrier conversion

Greek symbols

β	Heating rate for experimental tests, K/min
ω	Mass variation of oxygen carrier

Acronyms

AR	Air reactor
BET	Brunauer-Emmett-Teller
CLC	Chemical looping combustion
FR	Fuel reactor
ICSD	Inorganic crystal structure database
TGA	Thermogravimetric analyzer
TPR	Temperature programmed reduction
WGS	Water-Gas shift
XRD	X-ray diffraction

wastes possess the advantages of low cost. Nevertheless, minerals and industrial wastes always show lower reactivity than the synthetic ones in terms of coal combustion [17,18]. High reactivity of the synthetic oxygen carriers suggests a considerable decrease of materials inventory for CLC. In this context, a highly reactive Fe_2O_3/Al_2O_3 oxygen carrier was recently synthesized through sol-gel technique by Mei et al. [18]. During their tests in a fluidized bed reactor, the Fe_2O_3/Al_2O_3 oxygen carrier exhibited extremely high rates of char gasification and combustion over the other synthetic, mineral and industrial waste materials [18]. In this case, a very low solid inventory of around 600 kg/MW is adequate to reach a combustion efficiency of 99% at 1173 K.

For the further development of the sol-gel Fe_2O_3/Al_2O_3 oxygen carrier synthesized by Mei et al. [18], the reaction characteristics between the oxygen carrier and the gases involved in coal evolvement, i.e. CH_4, CO and H_2, must be thoroughly understood. Among them, the reaction kinetics is a basic tool for reactor design and modeling. Previous work determined the kinetics model for Fe_2O_3 reduction by H_2 based on a non-isothermal extrapolation method [19,20]. However, there is no work focused on the reaction kinetics of CO and the specific sol-gel Fe_2O_3/Al_2O_3 oxygen carrier. In fact, CO as a major component during the CLC of coals, its low reactivity with Fe_2O_3/Al_2O_3 dominates directly the concentration of CO_2 in the product gas stream, which finally affects the CO_2 capture. Although the Fe_2O_3/Al_2O_3 presents high reactivity with coal [18], the detailed reaction mechanism of CO and this oxygen carrier is not fully known. The knowledge of reaction kinetics of CO and Fe_2O_3/Al_2O_3 can assist the evaluation of reaction process, which can further be used to the optimization for full CO conversion to CO_2. More indeed, despite the Water-Gas Shift (WGS) reaction plays a role during the conversion of syngas-like (CO + H_2) fuels [21,22], the reactivity of this reaction may not be very relevant for kinetics model determination and oxygen carrier evaluation due to the low rate of WGS [23] and the origins of oxygen source from oxygen carrier instead of H_2O during CO combustion [21,22]. Therefore, the direct reaction of CO and oxygen carrier can be considered as a dominant pathway for CO combustion in syngas-like fuels. In this sense, it is highly necessary for the development of the kinetics model for the reduction of the sol-gel Fe_2O_3/Al_2O_3 and CO.

The objective of this work is to develop a kinetics model for the reduction of the sol-gel Fe_2O_3/Al_2O_3 oxygen carrier by CO. With this aim, thermodynamics calculations were first conducted to identify the dominant reactions for high CO_2 purity and no carbon formation, which is preferred in CLC. A series of experimental tests were carried out in a thermogravimetric analyzer (TGA) under various heating programs to understand the characteristics of Fe_2O_3/Al_2O_3 reduction by CO and to identify the main region for good CLC performance. Finally, based on the thermodynamic analysis, TGA tests and kinetics analysis, kinetics model was developed for the specific sol-gel Fe_2O_3/Al_2O_3 oxygen carrier during its reduction to Fe_3O_4/Al_2O_3 by CO.

2. Experimental

2.1. Oxygen carrier

The oxygen carrier particles are the same as that used in our previous work, which was concluded as a highly reactive material for CLC of coal [18]. This oxygen carrier containing 60 wt.% Fe_2O_3 and 40 wt.% Al_2O_3 was prepared through a sol-gel technique and calcined at 1473 K for 12 h in air. Detailed procedures of the oxygen carrier preparation can be found in our previous work [18]. Main properties of the fresh oxygen carrier are given in Table 1. The oxygen carrier particles were sieved to diameters of 0.125–0.180 mm, a desirable size for the fluidization in circulation fluidized beds. Crushing strength of the particles is the average strength for the fracture of 20 randomly-selected particles, measured by a Shimpo FGJ-5 apparatus, which is 1.39N and high enough for the use in fluidized beds [24]. The X-ray diffraction (XRD) patterns of the fresh and reduced materials were acquired in a Shimadzu 7000 diffractometer using a Ni-filtered Cu Kα radiation, which is presented in Fig. 1. The phase composition of the oxygen carrier was identified using the inorganic crystal structure database (ICSD). As shown in Fig. 1, the fresh oxygen carrier particles mainly contain Fe_2O_3 and Al_2O_3 phases. Real density of the material was determined in a Micromeritics AccuPyc 1330 picnometer, taking a value of 4653 kg/m^3. Specific surface area of the oxygen carrier particles is 1.39 m^2/g given by a Micromeritics ASAP2020 instrument according to the Brunauer–Emmett–Teller (BET) method. Finally, the oxygen transport capacity R_{OC} of the oxygen carrier was calculated as 0.02, considering the transformation from Fe_2O_3/Al_2O_3 to Fe_3O_4/Al_2O_3 during the reduction in this work.

Table 1
Main properties of the fresh Fe_2O_3/Al_2O_3 oxygen carrier.

Mass fraction of Fe_2O_3 (wt.%)	60
Particle size (mm)	0.125–0.180
Real density (kg/m^3)	4653
Crushing strength (N)	1.39
BET surface area (m^2/g)	1.39
Oxygen transport capacity, R_{OC}	0.02

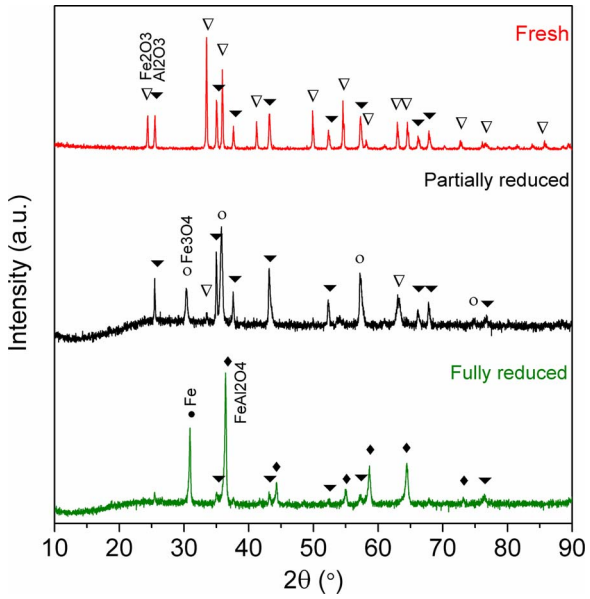

Fig. 1. XRD patterns of fresh, partially reduced and fully reduced oxygen carrier particles.

2.2. Thermogravimetric analysis

Reactions of the oxygen carrier and CO were carried out in a BOCI WCT-1D thermogravimetric analyzer (TGA) with a precision of 0.1 μg. More description of the TGA apparatus can be found elsewhere [25]. For each test, around 30 mg materials were loaded in the platinum plate in the atmosphere of 60 mL/min of 50%CO + 50%N_2 to avoid the effect of external film mass transfer and/or inter-particle diffusion [25]. Preliminary cyclic tests under various conditions were also conducted to observe the stability of the materials. However, neither deactivation nor activation of the oxygen carrier materials was noticed in cycles, thus the first reduction data was used for kinetics analysis. Generally, non-isothermal and isothermal methods can be both used for kinetics model development. However, in non-isothermal process reaction pathways can be more clearly identified, meanwhile synergy of different reactions can be avoided [26]. Moreover, the induction period of activation sites usually cannot be observed in isothermal process, due to the high reaction temperature [26]. With these considerations, non-isothermal method was introduced to carry out kinetics analysis. In order to obtain the kinetics information of the reaction, different heating rates $\beta = 3$–20 K/min were applied to raise the temperature of samples from room level to 1273 K.

3. Data evaluation

Oxygen transport capacity of the oxygen carrier, R_{OC}, represents the ability of oxygen transference for CLC process. In TGA tests, the value of R_{OC} can be obtained through Eq. (1), where m_{ox} and m_{red} are the weights of completely oxidized and reduced oxygen carriers, respectively. For the Fe_2O_3/Al_2O_3 oxygen carrier studied in this work, m_{ox} and m_{red} correspond to Fe_2O_3/Al_2O_3 and Fe_3O_4/Al_2O_3, respectively.

$$R_{OC} = \frac{m_{ox} - m_{red}}{m_{ox}} \tag{1}$$

In the TGA tests, the mass variation of the oxygen carrier, ω, is defined as the quotient between the instantaneous sample mass m and the fully oxidized sample mass m_{ox}, see Eq. (2).

$$\omega = \frac{m}{m_{ox}} \tag{2}$$

In the oxygen carrier studied, the available transformation for CLC is from Fe_2O_3/Al_2O_3 to Fe_3O_4/Al_2O_3 as discussed later in this work. Therefore, the solids conversion X was normalized for the above mentioned transformation, given by Eq. (3).

$$X = \frac{m_{ox} - m}{R_{OC} m_{ox}} \tag{3}$$

As stated above in Section 2, non-isothermal kinetics analysis possesses the advantages of clear identification of reaction pathways and induction process, as well as avoiding synergy reactions [26], therefore, this method was considered for kinetics analysis. In this case, a model-free isoconversion method proposed by Starink et al. [27] was introduced to determine the activation energy, E, for the reduction, see eq. 4 where T is the temperature at a fixed solids conversion, R is the universal gas constant and β is the heating rate. This method is recommended as an effective approximation by the ICTAC Kinetics Committee for the calculation of activation energy [28]. According to eq. 4, $\ln(\beta/T^{1.92})$ and $1/T$ must have a linear trend when experimental data was applied, which derived a fitted line at each conversion X. For

Table 2
Linear coefficient r^2 with respect to lg[$g(X)$] and $1/T$ in Eq. (2) for $0 < X \leq 0.5$, when various heating rates and $g(X)$ were used.

Model	$g(X)$	Linear coefficient r^2				
		β=3K/min	β=5K/min	β=10K/min	β=15K/min	β=20K/min
Avrami-Erofeev (1D)	-ln(1-X)	0.981	0.984	0.981	0.982	0.991
Avrami-Erofeev (2D)	[-ln(1-X)]$^{1/2}$	0.981	0.984	0.981	0.982	0.991
Avrami-Erofeev (3D)	[-ln(1-X)]$^{1/3}$	0.991	0.994	0.991	0.992	0.991
Diffusion (1D)	X^2	0.977	0.980	0.970	0.971	0.982
Diffusion (2D)	(1-X)·ln(1-X)+X	0.978	0.982	0.974	0.975	0.985
Diffusion (3D)	[1-(1-X)$^{1/3}$]^2	0.980	0.983	0.978	0.979	0.987
Power law	$X^{1/3}$, $X^{1/2}$, $X^{1/4}$, $X^{3/2}$	0.977	0.980	0.970	0.971	0.982
Contacting sphere	1-(1-X)$^{1/3}$	0.980	0.991	0.978	0.979	0.987
Contacting cylinder	1-(1-X)$^{1/2}$	0.980	0.982	0.976	0.977	0.986

■ r^2<0.98, ■ 0.98≤r^2≤0.99, □ r^2>0.99

instance, when $X = 0.1$ the temperatures T corresponding to this conversion for different tests at various ramp rates β can be obtained. Applying the T and the corresponding β to Eq. (4), the value of E at $X = 0.1$ can be determined via the slope of the fitted line between $\ln(\beta/T^{1.92})$ and $1/T$. For other conversions, the same rationale can be used to get the activation energies at different X. Finally, the activation energy can be determined as the arithmetic value for various X.

$$\ln\left(\frac{\beta}{T^{1.92}}\right) = -1.0008\cdot\left(\frac{E}{RT}\right) + \text{const} \tag{4}$$

The rate of solids conversion as a function of temperature, dX/dT, can be described as Eq. (5) where $f(X)$ is the differential form of model function for oxygen carrier conversion and A is the pre-exponential factor.

$$\frac{dX}{dT} = \frac{A}{\beta}\cdot\exp\left(-\frac{E}{RT}\right)\cdot f(X) \tag{5}$$

The model function $f(X)$ has an integral form $g(X)$, which has a relation with $f(X)$ as described in Eq. (6). Either model function, $f(X)$ or $g(X)$, represents the solids conversion term during the reaction process, which was usually developed experimentally according to the geometry of particles and the typical reaction characteristics. For a certain type of particle and reaction atmosphere, $f(X)$ as well as $g(X)$ is representative for the process. Based on large amount of investigations, a database was formed for the expressions of $f(X)$ and $g(X)$, which can be directly used for reaction kinetics model determination according to ICTAC Kinetics Committee [28]. Various expressions of $g(X)$ can be found in literatures [19,20,28–31], some of which are used in the present work for experimental data fitting as shown in Tables 2 and 3.

$$g(X) = \int_0^X \frac{1}{f(X)}dX \tag{6}$$

It should be pointed out that the eqs. 5 and 6 cannot be analytically solved; thereby some approximations were proposed to achieve reasonable estimation of this equation [28]. One of the most cited methods developed by Doyle et al. [32] as shown in Eq. (7) was used to determine the integral form of model function, $g(X)$. In this case, the expression of $g(X)$ presented in Tables 2 and 3 was used in Eq. (7) to see if a linear relation between $\lg[g(X)]$ and $1/T$ occurred. The $g(X)$ showed the best linear relation in Eq. (7) is confirmed as a suitable model to describe the reaction process after a full-scale comparison of model results and the experimental data.

$$\lg[g(X)] = \lg\left(\frac{AE}{RT}\right) - 2.315 - 0.4567\frac{E}{RT} \tag{7}$$

4. Thermodynamics

4.1. CO_2 purity

In this work, the oxygen carrier studied is composed of Fe_2O_3 and Al_2O_3, where the former component can be converted to Fe_3O_4, FeO and Fe by fuels. In the temperature programmed reduction (TPR) condition, successive reduction from Fe_2O_3 to Fe_3O_4, FeO and Fe can be clearly identified [26], as described in reactions R3-R6. Initially, Fe_2O_3 in the compound was reduced to Fe_3O_4 while Al_2O_3 was inert, as evidenced by the XRD pattern in Fig. 1. With the further reduction of Fe_3O_4, a new phase $FeAl_2O_4$ was formed as indicated in reaction R4 and the XRD pattern in Fig. 1. Because the content of Fe_2O_3, 60 wt.%, was excessive over the Al_2O_3 for the formation of $FeAl_2O_4$, free Fe_3O_4 was finally reduced to Fe phase, meanwhile Al_2O_3 was converted to $FeAl_2O_4$, as seen in XRD patterns of Fig. 1. It should be noted that the reduction of $FeAl_2O_4$ to Fe by CO was negligible at 673–1473 K according to the thermodynamics calculation and experimental results [26] as well as XRD tests in Fig. 1. In this sense, $FeAl_2O_4$ can be considered as an irreducible component during the reaction between CO and Fe_2O_3/Al_2O_3.

$$3Fe_2O_3 + Al_2O_3 + CO(g) \rightarrow 2Fe_3O_4 + Al_2O_3 + CO_2(g) \tag{R3}$$

$$Fe_3O_4 + 3Al_2O_3 + CO(g) \rightarrow 3FeAl_2O_4 + CO_2(g) \tag{R4}$$

$$Fe_3O_4 + CO(g) \rightarrow 3FeO + CO_2(g) \tag{R5}$$

$$FeO + CO(g) \rightarrow Fe + CO_2(g) \tag{R6}$$

For the reductions of Fe_3O_4 and FeO in reactions R5 and R6, the conversion of CO was much lower than 100%. As an example, Fig. 2 illustrated the incomplete conversion of CO during the reductions from Fe_3O_4 to FeO and then to Fe, determined by HSC Chemistry 6.1 [33]. According to the equilibrium composition in Fig. 2(a), the reaction between Fe_3O_4 and CO started at around 973 K which approached higher extents at increased temperatures. Despite this, the highest conversion of CO to CO_2 was still lower than 65% even at 1473 K. In the

Table 3
Linear coefficient r^2 with respect to $\lg[g(X)]$ and $1/T$ in Eq. (2) for $0.5 < X \leq 1$, when various heating rates and $g(X)$ were used.

Model	$g(X)$	Linear coefficient r^2				
		β=3K/min	β=5K/min	β=10K/min	β=15K/min	β=20K/min
Avrami-Erofeev (1D)	$-\ln(1-X)$	0.978	0.970	0.955	0.985	0.982
Avrami-Erofeev (2D)	$[-\ln(1-X)]^{1/2}$	0.978	0.970	0.955	0.985	0.982
Avrami-Erofeev (3D)	$[-\ln(1-X)]^{1/3}$	0.978	0.970	0.955	0.985	0.982
Diffusion (1D)	X^2	0.983	0.991	0.995	0.965	0.969
Diffusion (2D)	$(1-X)\cdot\ln(1-X)+X$	0.993	0.996	0.999	0.993	0.991
Diffusion (3D)	$[1-(1-X)^{1/3}]^2$	0.993	0.990	0.986	0.992	0.995
Power law	$X^{1/3}$, $X^{1/2}$, $X^{1/4}$, $X^{3/2}$	0.983	0.991	0.995	0.965	0.969
Contacting sphere	$1-(1-X)^{1/3}$	0.993	0.989	0.986	0.992	0.995
Contacting cylinder	$1-(1-X)^{1/2}$	0.939	0.994	0.994	0.991	0.995

■ $r^2<0.98$, ■ $0.98\leq r^2\leq 0.99$, □ $r^2>0.99$

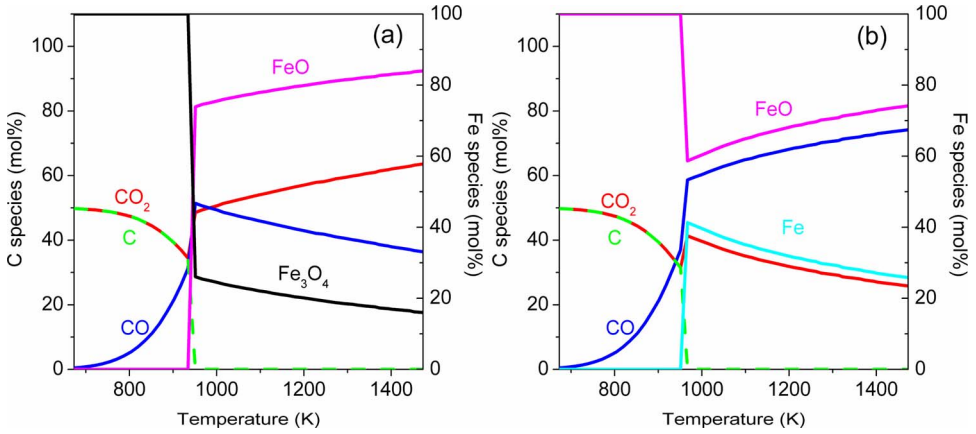

Fig. 2. Equilibrium composition for the reduction (a) from Fe_3O_4 to FeO and (b) from FeO to Fe by CO at 673–1473 K.

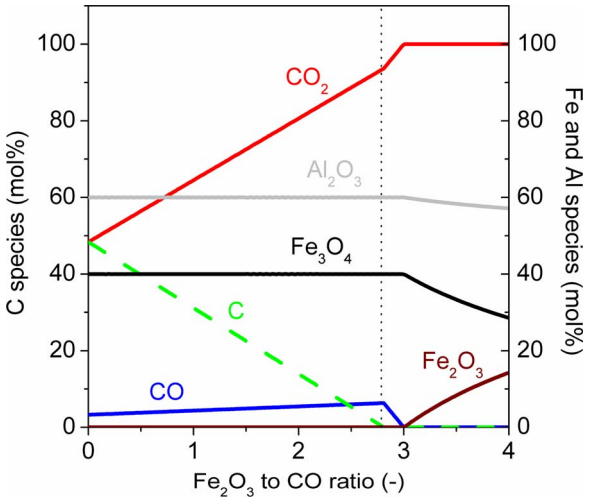

Fig. 3. Effects of Fe_2O_3 to CO ratio on the equilibrium composition for the reduction from Fe_2O_3/Al_2O_3 to Fe_3O_4/Al_2O_3 at 773 K.

case of FeO in Fig. 2(b), quite low conversion of CO was also encountered meanwhile higher temperature is more detrimental to the yield of CO_2. The decrease of CO conversion at higher temperatures for the reduction of FeO was due to the basic characteristics of thermodynamics, that is, higher temperature favors the endothermic reaction and lower temperature benefits the exothermic reaction. The reduction of FeO to Fe by CO is exothermic; thereby the increase of temperature was disadvantageous for the conversion of CO. Anyway, thermodynamics limitations were observed both for the reductions of Fe_3O_4 and FeO by CO, which is disadvantageous for the capture of CO_2. In this sense, the further reduction of Fe_3O_4 cannot be recommended for the application to CLC, which was also concluded elsewhere [34,35]. In contrast, for the reaction R3 where Fe_3O_4 and Al_2O_3 were the solid products, the CO conversion was always 100%, suggesting that a full CO_2 capture could be achieved in this case.

4.2. Carbon formation

During the circulation of oxygen carrier particles from FR to AR, carbon deposited on the particles could be conveyed to the AR where it is burnt to CO_2. This behavior can lead to the decrease of CO_2 capture efficiency of the entire CLC system, thus it is important to analyze if carbon is formed in the reaction of Fe_2O_3/Al_2O_3 and CO, as well as the strategies to avoid carbon formation. Two types of thermodynamics calculations were carried out to study the influences of temperature and oxygen carrier to fuel ratio on carbon formation, respectively.

Thermodynamics calculation was first performed under different temperatures while keeping the amount of reactants at stoichiometric ratio. In this way, the possible carbon formation can be evaluated within a wide interval of temperature. For the reduction from Fe_2O_3/Al_2O_3 to Fe_3O_4/Al_2O_3, i.e. reaction R3, carbon was never observed at any temperature. However, the further reductions of Fe_3O_4 to FeO and Fe were usually accompanied by carbon formation, which can be observed in Fig. 2. At temperatures between 673 and 973 K carbon was seen, but no reductions of Fe_3O_4 or FeO were found at the same time in Fig. 2. It is valuable to note that in Fig. 2 the fractions of carbon and CO_2 were identical, which decreased gradually to zero with the rise of temperature in the range of 673–973 K. In fact, the fractions of CO_2 and CO in Fig. 2 achieved the equilibrium compositions of Boudouard reaction at each temperature within 673–973 K. Consequently, the Boudouard reaction, reaction R7, was dominant for the formation of carbon, whereas the presence of Fe_3O_4 and FeO never showed any enhancement or inhibition to the carbon formation.

$$2CO(g) \leftrightarrow CO_2(g) + C \quad \text{(R7)}$$

In practical operation of a CLC system, the oxygen carrier to fuel ratio is difficult to be kept exactly at stoichiometric value meanwhile obtain high CO_2 capture efficiency. Thus, the second thermodynamics calculation was carried out using various values of Fe_2O_3 to CO ratio at constant temperatures to explore its influence on carbon formation. Fig. 3 depicted the evolution of C-, Fe- and Al- based species as a function of Fe_2O_3 to CO ratio at 773 K, a representative temperature of the reduction from Fe_2O_3/Al_2O_3 to Fe_3O_4/Al_2O_3 during the TPR process in TGA, see also Fig. 4. At such a temperature, the reaction between Fe_3O_4 and CO cannot assure the full conversion of CO according to the

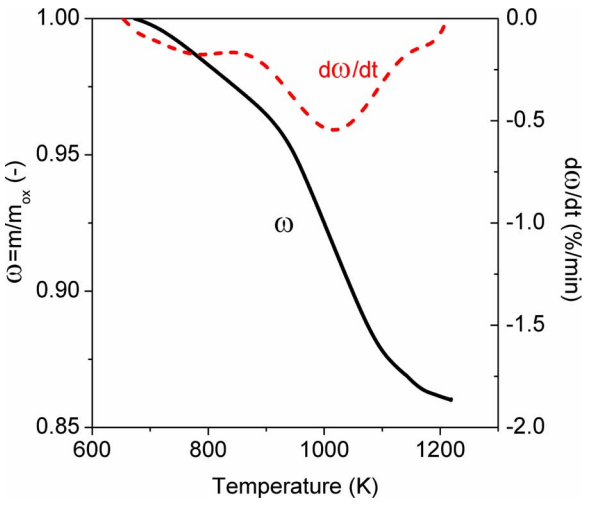

Fig. 4. Mass variation ω and $d\omega/dt$ for the reduction of Fe_2O_3/Al_2O_3 by CO with the temperature being increased from 673 to 1273 K at 10 K/min.

thermodynamics calculations in Fig. 2, so the reduction of oxygen carrier can only be limited to Fe_3O_4/Al_2O_3. In this sense, the thermodynamics analysis in this part was performed with respect to reaction R3 for oxygen carrier reduction and R7 for carbon formation. It can be seen in Fig. 3 that the carbon was formed at low Fe_2O_3 to CO ratios, e.g. lower than 2.8, suggesting that the reaction R7 was relevant under these conditions. With the increase of Fe_2O_3 to CO ratio, the fraction of carbon decreased linearly and finally reached zero when the Fe_2O_3 to CO ratio was higher than 2.8. Therefore, carbon formation could be possible at low Fe_2O_3 to CO ratios via the Boudouard reaction during the reduction of Fe_2O_3/Al_2O_3 to Fe_3O_4/Al_2O_3. However, it must be noted that carbon formation can be easily eliminated in practical operation by the elevation of reaction temperature and/or the addition of CO_2 and/or H_2O, possibly by recycling the residual heat of the exhaust gas streams of CLC reactors, to the FR.

5. Temperature programmed reduction (TPR)

As stated in Section 2, the non-isothermal method has the advantages of clear identifying the reaction pathways in terms of kinetics analysis, avoiding synergy reactions at high temperatures and showing induction period, especially for the Fe-based oxygen carrier which contains complicated reactions [26]. With this consideration, the non-isothermal process was used to determine the reaction kinetics models. In order to accomplish this purpose, the Fe_2O_3/Al_2O_3 oxygen carrier was reduced by CO until 1273 K at various temperature increasing rates β in the TGA. A representative reaction process is described in Fig. 4, where three steps can be identified according to the peaks of $d\omega/dt$ curve. At temperatures lower than 823 K, the $d\omega/dt$ peak could be related to the reduction of Fe_2O_3/Al_2O_3 to Fe_3O_4/Al_2O_3, of which Fe_3O_4 was subsequently reduced to FeO and Fe resulting in the peaks of $d\omega/dt$ at around 1000 and 1200 K, respectively. The formation of these phases in the reduction steps was evidenced by the XRD patterns shown in Fig. 1. For the fully reduced sample, Fe and $FeAl_2O_4$ were detected. Due to the three steps occurred at different temperatures, the rate of each reduction was not the same. In the end of reduction the mass variation was $\omega = 0.86$, which was lower than that corresponded to the reduction to Fe_3O_4/Al_2O_3, i.e. $R_{OC} = 0.02$, indicating the Fe_3O_4 was further reduced. In combination with the XRD results shown in Fig. 1, it can be found the final reduction products were Fe, $FeAl_2O_4$ and minor Al_2O_3. It should be noted that little reduction of $FeAl_2O_4$ occurred in the end of reaction with CO. In fact, less than 3% of $FeAl_2O_4$ was further converted to Fe, which suggested an extremely slow reaction of $FeAl_2O_4$ and CO even at temperatures close to 1273 K. This behavior confirmed that the reduction of $FeAl_2O_4$ and CO was negligible, which is in consistence with the XRD findings as seen in Fig. 1 and thermodynamics calculation not shown here. According to the calculations in the temperatures of 673–1473 K, negligible reduction of $FeAl_2O_4$ to Fe and Al_2O_3 by CO was also noticed. In this case, Fe, $FeAl_2O_4$ and minor amount of Al_2O_3 can be considered as the final products during the full reduction of Fe_2O_3/Al_2O_3 by CO. For the tests carried out at other heating rates, i.e. β = 3–20 K/min, the same consequence was obtained. However, only the reduction of Fe_2O_3/Al_2O_3 to Fe_3O_4/Al_2O_3 was considered for the kinetics analysis due to the limitations of good CLC performance for the further reduction of Fe_3O_4/Al_2O_3.

According to the thermodynamics analysis in *section 4*, carbon could be formed especially at low Fe_2O_3 to CO ratios and low temperatures, which is the case for the TPR process of Fe_2O_3/Al_2O_3 in the TGA because a continuous CO stream was passed through a small amount of oxygen carrier in the temperature increasing environment. In this sense, the Boudouard reaction was also evaluated experimentally with a blank test in a Micromeritics AutoChem II 2920 chemisorption analyzer, where CO was heated from room temperature to 1273 K at 10 K/min with highly pure quartz wool as inert bed material. Under this condition, there is no reaction between CO and the bed material, thus the Boudouard reaction can be examined at various temperatures. The evolution of CO in the gas stream is described in Fig. 5 as a function of temperature within the interval of 673–1273 K, where only one peak for CO consumption was detected. As discussed above, the consumption of CO for the blank test using highly pure quartz wool as bed material was attributable to the Boudouard reaction, which occurred at temperatures higher than 1000 K in the experimental case as seen in Fig. 5. However, according to the thermodynamics calculations carbon formation was predicted at much lower temperatures than 1000 K as shown in Figs. 2 and 3. The different behaviors of experimental tests and calculations might be attributed to the effects of reaction kinetics which was not considered during the thermodynamics analysis. Anyway, the temperature obtained experimentally for Boudouard reaction was much higher than that at the end of the reduction of Fe_2O_3/Al_2O_3 to Fe_3O_4/Al_2O_3 in TGA tests, see Fig. 4. Therefore, the conclusion can be drawn that carbon was never deposited on the oxygen carrier during the reduction to Fe_3O_4/Al_2O_3 in the TPR process of TGA tests due to the reaction temperatures in this stage were lower than 1000 K. In this case, the reduction from Fe_2O_3/Al_2O_3 to Fe_3O_4/Al_2O_3 during TGA tests was not influenced by carbon formation.

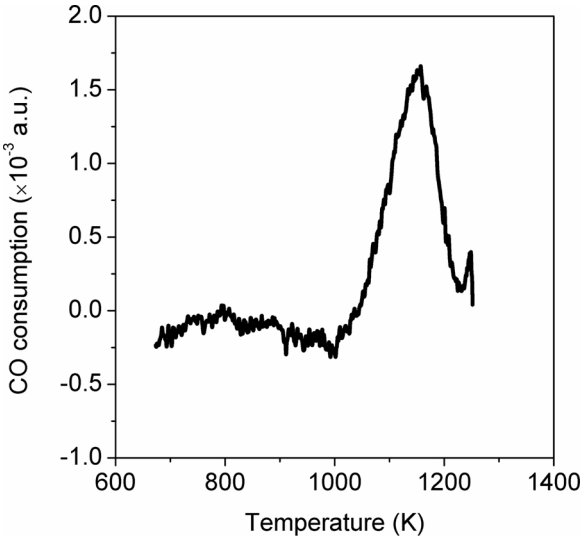

Fig. 5. Blank test of CO consumption as a function of temperature in the chemisorption analyzer with highly-pure quartz wool as bed material.

As a consequence, the TGA data obtained at 673–773 K corresponds to the conversion of Fe_2O_3/Al_2O_3 to Fe_3O_4/Al_2O_3 which was not affected by carbon formation from the Boudouard reaction. Another fact that needs to be stressed is the irrelevance of WGS reaction for kinetics determination of CO conversion during syngas-like combustion in CLC. This statement can be verified by: firstly, the lower rate of CO conversion via WGS with ilmenite as bed material, i.e. $1.67{\cdot}10^{-6}$–$4.16{\cdot}10^{-5}$ mol/((gram of ilmenite)·s) obtained by Ortiz et al. [23], than that of CO conversion by Fe_2O_3/Al_2O_3, i.e. $11.8–12.7{\cdot}10^{-5}$ mol/((gram of oxygen carrier)·s) calculated using the kinetics model determined later in the present work; secondly, the fact that oxygen source for CO and H_2 combustions in syngas comes mainly from oxygen carrier materials instead of H_2O steam that involved in WGS reaction [21,22]. In this sense, the following kinetics analysis carried out at the interval 673–773 K only corresponds to the reduction of Fe_2O_3/Al_2O_3 to Fe_3O_4/Al_2O_3 by CO, which would be significant for its use in CLC process.

6. Kinetics model

6.1. Activation energy

Because of the advantages of clear identifying reaction pathways, avoiding synergy reactions at high temperatures as well as showing

induction period [26], the present work applied the non-isothermal method and TPR data to determine the reaction kinetics. Table 4 lists the distribution of temperatures reached at given solid conversion and fixed heating rate. In general, all the reduction from Fe_2O_3/Al_2O_3 to Fe_3O_4/Al_2O_3 by CO was completed in the temperature range of 673–773 K. In Table 4, it is obvious that higher solids conversions were reached at higher temperatures under various heating rates. For a given value of X, the increase of heating rate also showed some positive effects on the increase of the temperature. This behavior can be ascribed to that the minimum reaction temperature for Fe_2O_3/Al_2O_3 and CO can be more easily reached at lower heating rates.

In order to obtain the activation energy, a model-free method proposed by Starink et al. [27] was used, which is shown in Eq. (4). At a given value of X in Table 4, $\ln(\beta/T^{1.92})$ was plotted against $1/T$ in Fig. 6. It can be seen in Fig. 6 that the relation of $\ln(\beta/T^{1.92})$ and $1/T$ for each X cannot be fitted by only one line. Instead, two segments can be observed in Fig. 6, which is divided by the rate β = 10 K/min. More indeed, this similar behavior was also noticed by Erri et al. [36] for the reduction of a Ni-based oxygen carrier with H_2 under various heating rates. They concluded that this phenomenon was attributed to different reaction mechanisms –intrinsic kinetics regime at low heating rates and internal diffusion control at intermediate heating rates–. Accordingly, the present work considered chemical reaction at lower heating rates and diffusion effect at higher heating rates as the dominant reaction mechanisms. For each conversion from 0.1 to 0.9 in Fig. 6 the linear coefficients r^2 with respect to the values of $\ln(\beta/T^{1.92})$ and $1/T$ for the two segments were both higher than 0.97, which suggested that the Eq. (4) was fulfilled at all the conversions studied. According to the slopes of the two linear fitting lines for $\ln(\beta/T^{1.92})$ and $1/T$, the activation energy for chemical reaction and diffusion control at each value of X can be calculated, respectively. It is noted that the difference of activation energy value for various solids conversions is lower than 25 kJ/mol. In this sense, the activation energy for the reduction of Fe_2O_3/Al_2O_3 to Fe_3O_4/Al_2O_3 was determined as the arithmetic average for the different conversions. For chemical reaction control, the activation energy was 270 kJ/mol, whereas for diffusion control this parameter took 131 kJ/mol.

6.2. Reduction mechanism function

After the determination of activation energy, a model fitting process proposed by Doyle et al. [32], see Eq. (7), was applied to find the model function $g(X)$ that can best describe the reduction from Fe_2O_3/Al_2O_3 to Fe_3O_4/Al_2O_3. The usually used kinetic models and the corresponding functions $g(X)$ recommended by the ICTAC Kinetics Committee [28] are gathered in Tables 2 and 3, which were taken into account in the present work. Using the $g(X)$ values calculated at various conversions and temperatures derived from TGA tests, the linear coefficient r^2 between $\lg[g(X)]$ and $1/T$ based on eq. 7 was obtained, which are shown in Tables 2 and 3. However, during the correlation between $\lg[g(X)]$ and $1/T$, it was found that the conversion X must be divided into two segments, i.e. $0 < X \leq 0.5$ and $0.5 < X \leq 1$, to give good linear relation between $\lg[g(X)]$ and $1/T$, which was due to the different dominant mechanisms for the reduction process, as stated below. In the case of $0 < X \leq 0.5$ as shown in Table 2, it was found that the values of

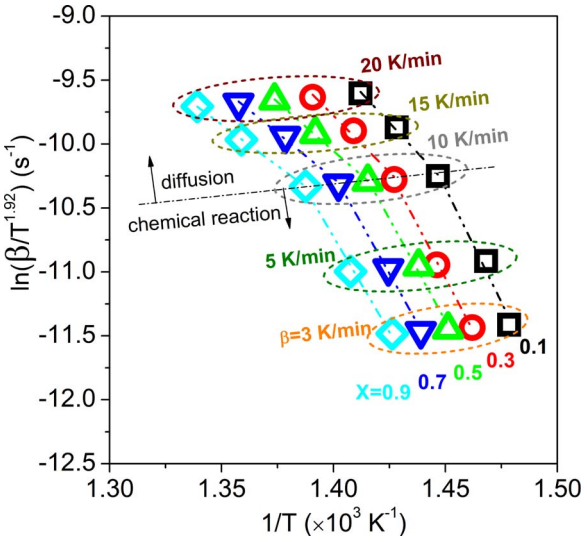

Fig. 6. Determination of activation energy E for the reduction of Fe_2O_3/Al_2O_3 to Fe_3O_4/Al_2O_3 by CO using the Starink method [27] considering chemical reaction at low heating rates (β = 3–10 K/min) and diffusion mechanism at high heating rates (β = 10–20 K/min).

r^2 were distributed between 0.970 and 0.994 for all the expressions of $g(X)$ considered. The power law model has the lowest preciseness for the description of the reduction from Fe_2O_3/Al_2O_3 to Fe_3O_4/Al_2O_3, since the corresponding values of r^2 were always smaller than 0.982. For the diffusion model, contacting sphere model and contacting cylinder model, unsatisfactory predictions of the experiments performed at β = 10 K/min and β = 15 K/min were encountered. In this sense, these kinetic models were not suitable for the description of the reduction from Fe_2O_3/Al_2O_3 to Fe_3O_4/Al_2O_3 by CO. Differently, the Avrami-Erofeev model with various dimensions, i.e. 1D, 2D and 3D, presented good linear relation of $\lg[g(X)]$ and $1/T$, which suggested the possible feasibility of using this type of model to describe the reaction for $0 < X \leq 0.5$. In the case of $0.5 < X \leq 1$ as shown in Table 3, the Avrami-Erofeev models showed values of r^2 smaller than 0.985. For power law models, unsatisfactory linear relationships of $\lg[g(X)]$ and $1/T$ were also observed. In comparison to the above two types of models, diffusion model, contacting sphere model and the contacting cylinder model have better correlations of $\lg[g(X)]$ and $1/T$. Among them, the 2D diffusion model $g(X) = (1\text{-}X)\cdot\ln(1\text{-}X) + X$ exhibited the highest values of r^2 for all the heating rates.

In order to confirm the linear relation of $\lg[g(X)]$ and $1/T$ in the whole process of the reduction from Fe_2O_3/Al_2O_3 to Fe_3O_4/Al_2O_3, the models were examined for all the solids conversions and the corresponding temperatures. Fig. 7 shows the full scale comparison when 1D Avrami-Erofeev model, 3D Avrami-Erofeev model, 2D diffusion model and contacting sphere model were considered for $0 < X \leq 0.5$ and $0.5 < X \leq 1$, respectively. It can be seen that at lower temperatures the 1D Avrami-Erofeev model $g(X) = -\ln(1\text{-}X)$, 2D diffusion model $g(X) = (1\text{-}X)\cdot\ln(1\text{-}X) + X$ and contacting sphere model $g(X) = 1\text{-}(1\text{-}X)^{1/3}$ exhibited a non-linear relation of $\lg[g(X)]$ and $1/T$. On the contrary, the 3D Avrami-Erofeev model $g(X) = [-\ln(1\text{-}X)]^{1/3}$ showed the best linear

Table 4
Temperature distribution T(K) at various solid conversions X and heating rates β.

Solids conversion	β = 3 K/min	β = 5 K/min	β = 10 K/min	β = 15 K/min	β = 20 K/min
X = 0.1	676	684	694	700	708
X = 0.3	684	699	706	710	719
X = 0.5	689	705	715	718	728
X = 0.7	695	712	720	725	737
X = 0.9	701	720	727	736	747

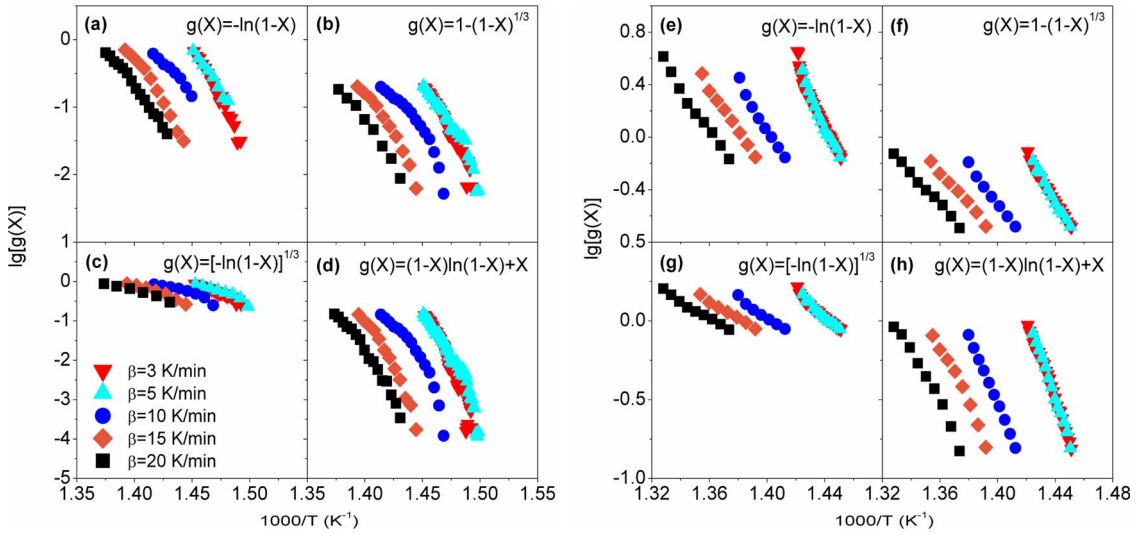

Fig. 7. Full scale comparison of linear relation between lg[$g(X)$] and $1/T$ at various heating rates β when 1D Avrami-Erofeev model, 3D Avrami-Erofeev model, 2D diffusion model and contacting sphere model were used for (a–d) $0 < X \leq 0.5$ and (e–h) $0.5 < X \leq 1$.

relation in the full scale of $0 < X \leq 0.5$ and T for the reduction of Fe_2O_3/Al_2O_3 to Fe_3O_4/Al_2O_3 at various heating rates. Then, the pre-exponential factor A can be determined from the interception of Eq. (7) using $g(X) = [-\ln(1-X)]^{1/3}$ and $E = 270$ kJ/mol, which took a value of $1.6 \cdot 10^{12}\,s^{-1}$. With regard to $0.5 < X \leq 1$, 2D diffusion model $g(X) = (1-X)\cdot\ln(1-X) + X$ showed the best linear relation, according to which the pre-exponential factor in this stage was determined as $3.1 \cdot 10^{3}\,s^{-1}$.

Although in Fig. 7 the best linear relation between lg[$g(X)$] and $1/T$ is observed at various heating rates, it is necessary to compare the model results with the experimental data in terms of oxygen carrier conversion. Therefore, Fig. 8 shows the model prediction and the experimental results under various heating rates. Clearly, the model exhibits sufficient accuracy for the prediction of experimental data, which indicates that the model functions $g(X) = [-\ln(1-X)]^{1/3}$, $g(X) = (1-X)\cdot\ln(1-X) + X$ and the corresponding kinetics parameters are reliable for the description of the reduction from Fe_2O_3/Al_2O_3 to Fe_3O_4/Al_2O_3 by CO.

6.3. Reaction process description with the kinetics model

According to the 3D Avrami-Erofeev model $g(X) = [-\ln(1-X)]^{1/3}$ and the 2D diffusion model $g(X) = (1-X)\cdot\ln(1-X) + X$, the reduction of Fe_2O_3/Al_2O_3 to Fe_3O_4/Al_2O_3 can be described as a 3D nucleation and nuclei growth process followed by a 2D diffusion control, as shown in Fig. 9. After the induction period, nuclei of Fe_3O_4 were formed in a 3D manner, as seen in Fig. 9(a). Then, the growth of Fe_3O_4 nuclei and the formation of new Fe_3O_4 nuclei occurred simultaneously; see Fig. 9(b). With the reduction of oxygen carrier, the Fe_3O_4 nuclei grew larger and then overlapped to form the nucleation in Fig. 9(c). Afterwards, the Fe_3O_4 nucleation ingested the smaller nucleation sites in Fig. 9(d) to form bigger nucleation. The Fe_3O_4 sites were eventually constructed after continuing Fe_3O_4 nuclei growth and Fe_3O_4 nucleation formation

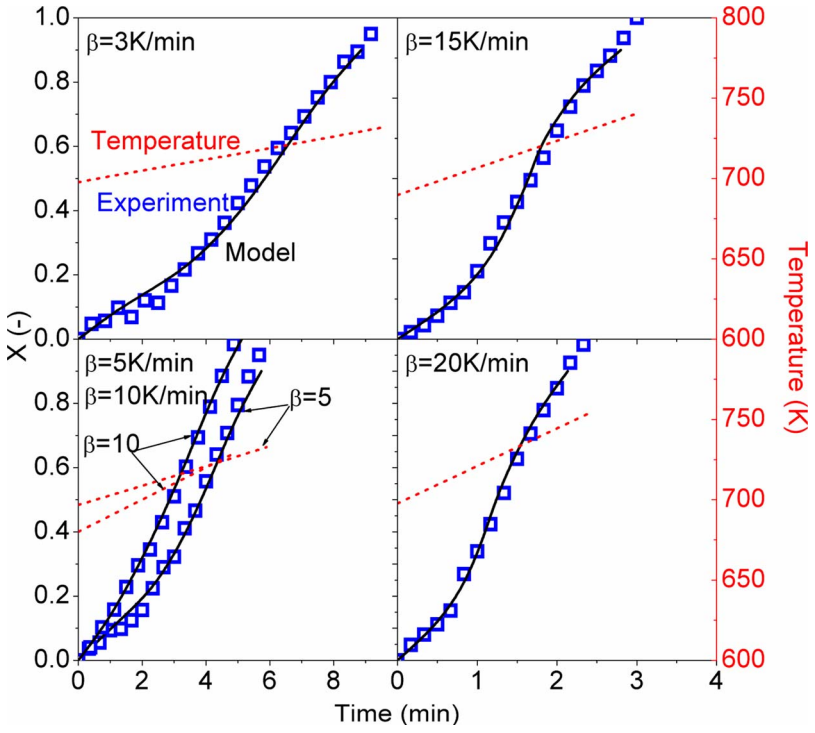

Fig. 8. Comparison of model predictions and experimental solids conversions for the reduction from Fe_2O_3/Al_2O_3 to Fe_3O_4/Al_2O_3 by CO at various heating rates.

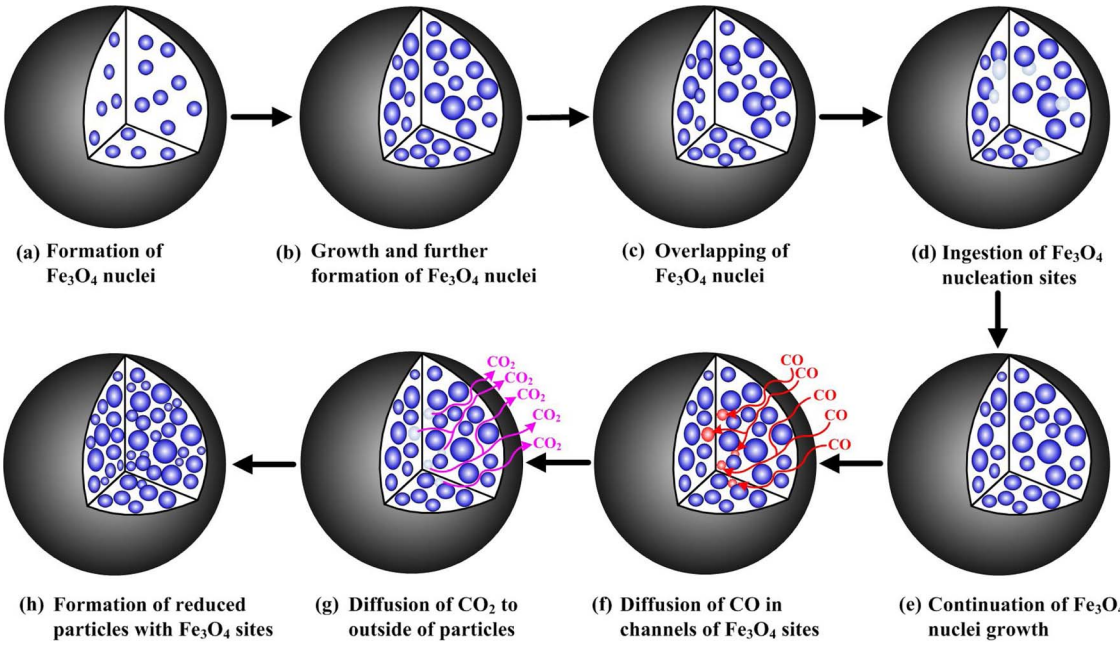

Fig. 9. The 3D nucleation and nuclei growth process of Fe_3O_4 followed by 2D diffusion control during the reduction of Fe_2O_3/Al_2O_3 by CO, including formations of Fe_3O_4 nuclei or nucleation (●), partially ingested Fe_3O_4 nucleation (●), gases bypass through products channels (pink and red lines). (For interpretation of the references to colour in this figure legend, the reader is referred to the web version of this article.)

as illustrated in Fig. 9(e). With the increase of Fe_3O_4 sites in the oxygen carrier particles, reactant and product gases (CO and CO_2) have to pass through the channels between sites, which changed reaction mechanism to 2D diffusion control, that is, the diffusion via the vertical direction of the reaction surfaces, as illustrated in Fig. 9(f–g). Finally, in Fig. 9(h) after the full reduction of Fe_2O_3 to Fe_3O_4, the Fe_3O_4 sites joined together to form the reduced oxygen carrier particles.

7. Conclusion

The previously investigated sol-gel Fe_2O_3/Al_2O_3 oxygen carrier was studied in this work focusing on the development of reaction kinetics model for the reduction by CO. In order to derive reliable kinetics model, thermodynamics analysis was first performed to identify the preferred region for CLC operation. Afterward, temperature programmed reduction (TPR) tests were carried out in a thermogravimetric analyzer (TGA) to find the available reaction process for kinetics model development.

According to the thermodynamics calculation, the available system to gain high purity of CO_2 for CLC corresponds to the conversion of Fe_2O_3/Al_2O_3 to Fe_3O_4/Al_2O_3. Further reduction will lead to carbon formation and lower CO_2 capture. However, in experimental case, the carbon formation was never detected at temperatures lower than 1000 K which might be attributable to the kinetics of Boudouard reaction. During the TPR tests, the oxygen carrier was reduced to Fe_3O_4/Al_2O_3 at temperatures of 673–773 K and various heating rates in TGA. Based on a non-isothermal analysis in this temperature interval, a 3D Avrami-Erofeev model with the model function $g(X) = [-\ln(1-X)]^{1/3}$ and activation energy 270 kJ/mol was confirmed suitable for the description of the first half of Fe_2O_3/Al_2O_3 reduction to Fe_3O_4/Al_2O_3, i.e. $0 < X \leq 0.5$. The pre-exponential factor using this model was determined as $1.6 \cdot 10^{12}\ s^{-1}$. After that, the rest reduction, i.e. $0.5 < X \leq 1$, from Fe_2O_3/Al_2O_3 to Fe_3O_4/Al_2O_3 was dominant by a 2D diffusion model $g(X) = (1-X)\cdot\ln(1-X) + X$. The activation energy and pre-exponential factor for this stage were 131 kJ/mol and $3.1 \cdot 10^{3}\ s^{-1}$, respectively. According to the developed kinetics model, the reduction of the oxygen carrier initiated via a 3D nucleation and nuclei growth process to form the nucleation of Fe_3O_4, which was followed by the diffusion of reactant and product gases (CO and CO_2) through channels among Fe_3O_4 sites. Finally, the reduced oxygen carrier particles were generated by the combination of the above mentioned active sites.

Acknowledgement

This research was partially supported by National Key R&D Program of China (2016YFB0600801), National Natural Science Foundation of China (51576077 and 51376078), Fundamental Research Funds for the Central Universities (2662016QD043, 2015PY077).

References

[1] IEA, World Energy Outlook, OECD/IEA, Paris, 2013, p. 2013.
[2] R.K. Pachauri, M. Allen, V. Barros, J. Broome, W. Cramer, R. Christ, J. Church, L. Clarke, Q. Dahe, P. Dasgupta, Synthesis Report. Contribution of Working Groups I, II and III to the Fifth Assessment Report of the Intergovernmental Panel on Climate Change, (2014).
[3] D. Archer, Fate of fossil fuel CO_2 in geologic time, J. Geophys. Res.: Oceans 110 (2005) 1–6.
[4] H.R. Kerr, Capture and separation technology gaps and priority research needs, in: D.C. Thomas (Ed.), Carbon Dioxide Capture for Storage in Deep Geologic Formations, Elsevier Science, Amsterdam, 2005, pp. 655–660.
[5] W.K. Lewis, E.R. Gilliland, Production of pure carbon dioxide, US Patent 2,665,971, 1954.
[6] J. Richter Horst, F. Knoche Karl, Reversibility of combustion processes, in: R. Gaggioli (Ed.), Efficiency and Costing, ACS Symp. Ser, 1983, pp. 71–85.
[7] M. Ishida, D. Zheng, T. Akehata, Evaluation of a chemical-looping-combustion power-generation system by graphic exergy analysis, Energy 12 (1987) 147–154.
[8] J. Adánez, A. Abad, F. García-Labiano, P. Gayán, L.F. de Diego, Progress in chemical-Looping combustion and reforming technologies, Prog. Energy Combust. Sci. 38 (2012) 215–282.
[9] A. Cuadrat, A. Abad, F. García-Labiano, P. Gayán, L.F. de Diego, J. Adánez, The use of ilmenite as oxygen-carrier in a 500W_{th} Chemical-Looping Coal Combustion unit, Int. J. Greenhouse Gas Control 5 (2011) 1630–1642.
[10] N. Berguerand, A. Lyngfelt, Design and operation of a 10 kW_{th} chemical-looping combustor for solid fuels – testing with South African coal, Fuel 87 (2008) 2713–2726.
[11] P. Markström, C. Linderholm, A. Lyngfelt, Operation of a 100 kW chemical-looping combustor with Mexican petroleum coke and Cerrejón coal, 2nd Int Conf. on Chemical Looping, Darmstadt, 2012.
[12] J. Ströhle, M. Orth, B. Epple, Design and operation of a 1MW_{th} chemical looping plant, Appl. Energy 113 (2014) 1490–1495.
[13] A. Abad, R. Pérez-Vega, L.F. de Diego, F. García-Labiano, P. Gayán, J. Adánez, Design and operation of a 50 kW_{th} Chemical Looping Combustion (CLC) unit for solid fuels, Appl. Energy 157 (2015) 295–303.

[14] T. Mendiara, F. García-Labiano, P. Gayán, A. Abad, L.F. de Diego, J. Adánez, Evaluation of the use of different coals in Chemical Looping Combustion using a bauxite waste as oxygen carrier, Fuel 106 (2013) 814–826.
[15] T. Song, T. Shen, L. Shen, J. Xiao, H. Gu, S. Zhang, Evaluation of hematite oxygen carrier in chemical-looping combustion of coal, Fuel 104 (2013) 244–252.
[16] S. Zhang, C. Saha, Y. Yang, S. Bhattacharya, R. Xiao, Use of Fe_2O_3-containing industrial wastes As the oxygen carrier for chemical-looping combustion of coal: effects of pressure and cycles, Energy Fuels 25 (2011) 4357–4366.
[17] A. Abad, A. Cuadrat, T. Mendiara, F. García-Labiano, P. Gayán, L.F. de Diego, J. Adánez, Low-Cost Fe-Based oxygen carrier materials for the *i*G-CLC process with coal. 2, Ind. Eng. Chem. Res. 51 (2012) 16230–16241.
[18] D. Mei, A. Abad, H. Zhao, J. Adánez, C. Zheng, On a highly reactive Fe_2O_3/Al_2O_3 oxygen carrier for in situ gasification chemical looping combustion, Energy Fuels 28 (2014) 7043–7052.
[19] H. Zhao, D. Mei, J. Ma, C. Zheng, Comparison of preparation methods for iron-alumina oxygen carrier and its reduction kinetics with hydrogen in chemical looping combustion, Asia-Pac. J. Chem. Eng. 9 (2014) 610–622.
[20] H. Tian, Q. Guo, J. Chang, Investigation into decomposition behavior of $CaSO_4$ in chemical-looping combustion, Energy Fuels 22 (2008) 3915–3921.
[21] C.R. Forero, P. Gayán, L.F. de Diego, A. Abad, F. García-Labiano, J. Adánez, Syngas combustion in a 500 W_{th} Chemical-Looping Combustion system using an impregnated Cu-based oxygen carrier, Fuel Process. Technol. 90 (2009) 1471–1479.
[22] C. Dueso, F. García-Labiano, J. Adánez, L.F. de Diego, P. Gayán, A. Abad, Syngas combustion in a chemical-looping combustion system using an impregnated Ni-based oxygen carrier, Fuel 88 (2009) 2357–2364.
[23] M. Ortiz, F. Gallucci, T. Melchiori, V. Spallina, M. van Sint Annaland, Kinetics of the reactions prevailing during packed-bed chemical looping combustion of syngas using ilmenite, Energy Technol. 4 (2016) 1137–1146.
[24] M. Johansson, T. Mattisson, A. Lyngfelt, Investigation of Fe_2O_3 with $MgAl_2O_4$ for chemical-looping combustion, Ind. Eng. Chem. Res. 43 (2004) 6978–6987.
[25] L. Guo, H. Zhao, K. Wang, D. Mei, Z. Ma, C. Zheng, Reduction kinetics analysis of sol–gel-derived $CuO/CuAl_2O_4$ oxygen carrier for chemical looping with oxygen uncoupling, J. Therm. Anal. Calorim. 123 (2015) 745–756.
[26] A. Cabello, A. Abad, F. García-Labiano, P. Gayán, L.F. de Diego, J. Adánez, Kinetic determination of a highly reactive impregnated Fe_2O_3/Al_2O_3 oxygen carrier for use in gas-fueled Chemical Looping Combustion, Chem. Eng. J. 258 (2014) 265–280.
[27] M.J. Starink, The determination of activation energy from linear heating rate experiments: a comparison of the accuracy of isoconversion methods, Thermochim. Acta 404 (2003) 163–176.
[28] S. Vyazovkin, A.K. Burnham, J.M. Criado, L.A. Pérez-Maqueda, C. Popescu, N. Sbirrazzuoli, ICTAC Kinetics Committee recommendations for performing kinetic computations on thermal analysis data, Thermochim. Acta 520 (2011) 1–19.
[29] M. Arjmand, M. Keller, H. Leion, T. Mattisson, A. Lyngfelt, Oxygen release and oxidation rates of $MgAl_2O_4$-Supported CuO oxygen carrier for chemical-looping combustion with oxygen uncoupling (CLOU), Energy Fuels 26 (2012) 6528–6539.
[30] K. Wang, Q. Yu, Q. Qin, Reduction kinetics of Cu-based oxygen carriers for chemical looping air separation, Energy Fuels 27 (2013) 5466–5474.
[31] H. Song, K. Shah, E. Doroodchi, T. Wall, B. Moghtaderi, Analysis on chemical reaction kinetics of CuO/SiO_2 oxygen carriers for chemical looping air separation, Energy Fuels 28 (2014) 173–182.
[32] C.D. Doyle, Estimating isothermal life from thermogravimetric data, J. Appl. Polym. Sci. 6 (1962) 639–642.
[33] A. Roine, HSC Chemistry 6.1: Chemical Reaction and Equilibrium Software with Thermochemical Database and Simulation Module, Oututec Research Oy, 2008.
[34] E. Jerndal, T. Mattisson, A. Lyngfelt, Thermal analysis of chemical-looping combustion, Chem. Eng. Res. Des. 84 (2006) 795–806.
[35] T. Mattisson, A. Lyngfelt, Capture of CO_2 using chemical-looping combustion, 1st Biennial Meeting of the Scandinavian-Nordic Section of the Combustion Institute, Göteborg, April 2001, 2001.
[36] P. Erri, A. Varma, Diffusional effects in nickel oxide reduction kinetics, Ind. Eng. Chem. Res. 48 (2009) 4–6.